Role of preplaced silicon on a TIG processed SiC incorporated microalloyed steel

*T.N. Baker[1], P. Munoz de Escalona[2], M Olasolo[3], T. Marrocco[3], J. Kelly[1] , B.Wei[4], K. He[4], S. Mridha[1].

[1]Department of Mechanical and Aerospace Engineering, James Weir Building, University of Strathclyde, Glasgow G1 1XJ, UK

[2] School of Computing, Engineering and Built Environment. Glasgow Caledonian University, Glasgow, G4 0BA

[3]Advanced Materials Research Laboratory
University of Strathclyde, Glasgow, G1 1XJ, UK

[4] Electron Microscopy Laboratory
Advanced Research Centre,
Central South University,
Changsha, 41083,
Hunan, China.

neville. baker @strath.ac.uk *Corresponding author
patricia.munoz@gcu.ac.uk
m.olasolo@strath.ac.uk
t.Marrocco@strath.ac.uk
j. kelly@strath.ac.uk
bingqiang.wei@csu.edu.cn.
k. he 何克坚 cbbr16@126.com
shahjahanmridha@gmail.com

This is a peer reviewed, accepted author manuscript of the following research article:

Baker, T. N., Muñoz-de Escalona, P., Olasolo, M., Marrocco, T., Kelly, J., Wei, B., He, K., & Mridha, S. (2020). Role of preplaced silicon on a TIG processed SiC incorporated microalloyed steel. *Materials Science and Technology*, 36(12), 1349-1363. https://doi.org/10.1080/02670836.2020.1781355

Abstract

Research aimed at enhancing the surface properties of carbon steels by incorporating fine silicon carbide particulates has had limited success because dissolution of the ceramic occurred. This research considers a method of reducing SiC dissolution by generating a high Fe-Si liquid which protects the ceramic. Three particulate groups were investigated, (1) ~ 5µm SiC, (2) ~45µm Si +~ 5µm SiC, and (3) ~45µm Si, all incorporated into a microalloyed steel using a TIG process. Detailed microhardness of the melt zones together with XRD and analytical SEM showed that the addition of Si resulted in a cracked hard layer containing SiC. However, a thicker, harder crack- free layer resulted from the microstructure developed by the dissolution of SiC.

Key words: Surface engineering; microalloyed steel; silicon carbide and silicon particulates; TIG melting; microhardness; XRD; SEM.

Introduction

The development of improved wear resistance through the incorporation of ceramic particulates such as SiC, has been achieved in bulk metal matrix composites [1, 2]. This is also well established in aluminum and titanium alloy surfaces through laser processing [3-6]. Lasers have been used to clad [7, 8] and surface melt mild steels, [7,9-11] resulting in an increase in the hardness of t a crack-free melt zone through assimilation of ceramics [10]. An alternative source of surface melting to lasers is by the more economical tungsten inert gas (TIG) process, which received some early attention for titanium alloys [12-14]. High tonnage applications in agriculture, mining, civil engineering and transportation for example [15-19], require relatively cheap methods of surface engineering of steels, to develop a combination of good toughness and abrasive wear resistance. The application of TIG to incorporate ceramics, such as TiC [20-22] and SiC particulates [23-25] into the surface regions of steels has been

investigated using a range of energy inputs and ceramic concentrations. Significant increases of 3 to 5 times of the hardness in the melt zone (MZ) after TIG processing have been recorded [10,23, 24,26,27].

Many compounds have been identified in research investigating SiC mixing with iron or low carbon steels. There are indications that SiC does not react with Fe below 1100°C (1373K).However, several studies have recorded the dissolution or partial dissolution of SiC particulates during surface engineering investigations involving laser or TIG processing, [28-35].

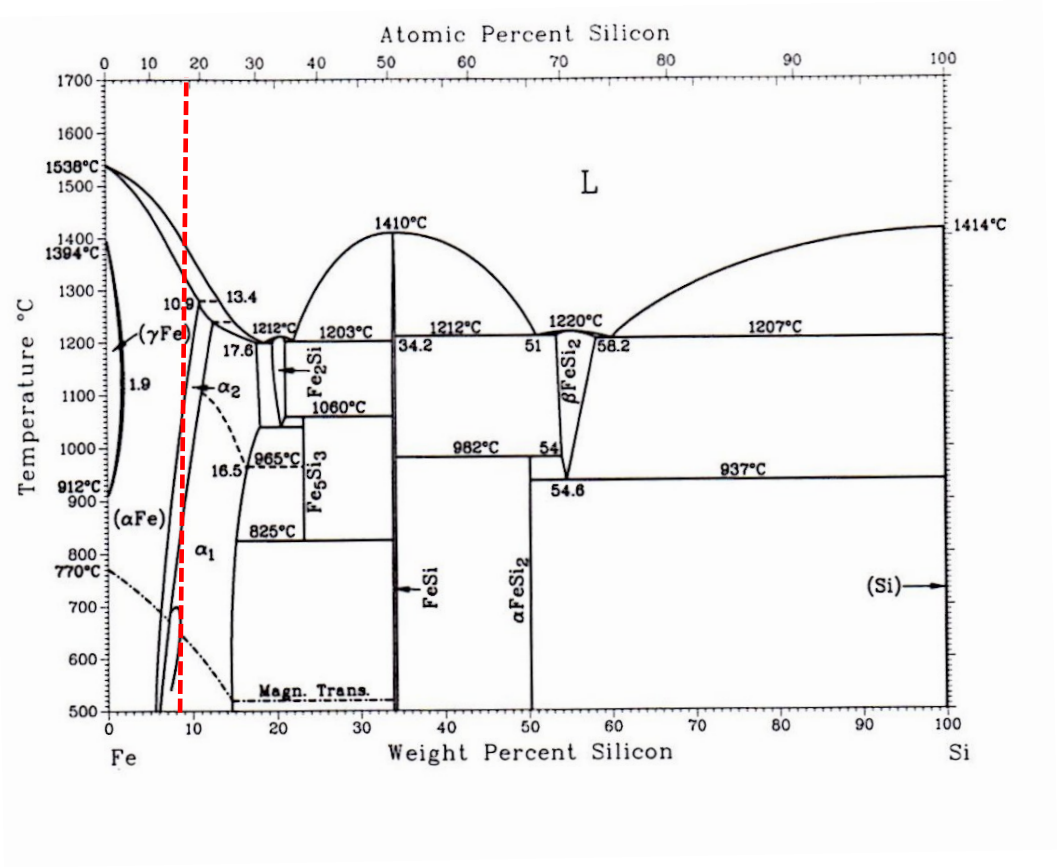

1 The Fe-Si equilibrium phase diagram after [36]

Figure 1 near here

The Fe-Si equilibrium phase diagram [36], Figure 1, shows that there exist several iron silicides, two which are stable below ~800°C (1073K),ε- FeSi (~33wt.% Si) and β-$FeSi_2$ (~50

wt.%Si).Other metastable phases are Fe_3Si, a DO_3 structure with a wide range of homogeneity, α-$FeSi_2$ and Fe_5Si_3, the latter two being high temperature phases. Several of these iron silicides have been characterized through XRD spectra [27-35,37]. Ohnuma et al. [38] have added important revisions to the miscibility gaps between the A2/B2 and B2/DO_3 phases, while more recently, a reassessment of the complete Fe-Si system by Cui and Jung [39] claims to provide a more accurate description than previously available.

The interface in Fe-SiC metal matrix composites was studied by Pelleg [29],with the aim of understanding the effect of SiC on cooling from austenite, a topic pertainent to the present research. Sintering and hot isostatic pressing of the mixed powders in the range at 1050°C (1323K) resulted in a thin 2 μm reaction layer between SiC and the matrix.Through SEM-EDS analysis, it was observed that the interface consisted of three layers, which were considered to be $FeSi_2$,FeSi and Fe_3Si respectively [29]. The solid state reaction zone between silicon carbide and iron has been studied in the temperature range from 800 to1100°C (1073 to 1373K) by Tang et al. [30], who concluded that Fe diffusion in Fe_3Si was the dominating diffusion species of the reaction. In general, the iron silicides are considered to be deleterious to the properties of the interface formed between SiC and iron, and should be avoided. This observation arises from the knowledge that the two ordered phases, B2 and DO_3 are considered to be highly brittle, resulting the well- established difficulties in cold rolling of Fe-6.5wt.%Si sheets [31].

Several attempts have been made to prevent the dissolution or partial dissolution of SiC particulates in iron and steels. Terry and Chinyamakobvu [28] found that potential protective *in situ* coatings of TiC or Al_2O_3 on SiC in liquid iron were unsuccessful, neither was the pre-coating of SiC with Ni and/or Cu. Unprotected SiC also reacted readily with iron in the solid state,1000–1200 °C (1273-1373K). However, pre-coating with Ni, did provide protection, preventing SiC dissolution and silicide formation during sintering at

these temperatures [28]. The effect of chromium additions in inhibiting the reaction between SiC and Fe was investigated by Tang et al. [32], but with limited success.

None of these approaches promised to be successful when surface engineering steels using TIG, where temperatures > 2700°C (>3000K) can be reached for short times.

The carbon-iron-silicon system has been reviewed by Raghaven and Ghosh[40], revised by the work of Lacaze and Sundman [41] which was up-dated by Miettinen [42]. The A2-B2 ordering reaction of the bcc phase was included but not an assessment of the DO_3 ordering [41,42]. More recently Kawanishi et al. [44] studied the equilibrium phase relationship between SiC and a liquid phase in the Fe-Si-C system at 1250-1450°C (1523-1723K). They found that Fe-36mol% Si alloy equilibrates with SiC at these temperatures and their results indicated that SiC is far more soluble in iron-rich Fe-Si melt than in a silicon rich melt. Kawanishi et al. [44] concluded that a melt of composition Fe-22wt.%Si, possessed a high SiC solubility and should be a suitable solvent for the rapid liquid phase growth of SiC. This conclusion is not considered to be influenced by more recent evaluations of the Fe-C-Mn-Si alloys [44,45].

The influence of C and Mn on the B2, DO_3 or B2 + DO_3 phase fields has received little attention in the literature. For the C and Mn levels reported in the present work, it is considered appropriate to discuss the microstructure as based on the binary Fe-Si system. Previous work by the present authors confirmed the complete dissolution of SiC particulates during the TIG surface engineering of a microalloyed steel [27]. However, this still resulted in ~ four - fold increase in the hardness of the TIG processed melt zone, considered to be due mainly to the formation of a martensitic phase.

The current research investigated the potential of developing even higher hardness levels in the MZ, by overcoming the dissolution of SiC and retaining the particulates through increasing the silicon content in this region. In the present TIG processing investigation, a

layer of silicon particulates was placed next to the steel, with the intention of forming a high Fe-Si-C liquid phase, before a second layer comprised of ~ 5µm SiC particulates was incorporated into the melt. An energy input of 420Jmm^{-1} was used, selected as the optimum in a previous project [27] for achieving a high hardness to a depth >1mm without porosity or cracking.

Experimental

A surface engineering technique based on a tungsten inert gas (TIG) torch was used to study the influence of Si+ SiC powder on the microstructure and hardness of a microalloyed (MA) steel. The composition of the MA steel base metal (BM), 0.14C-1.26Mn-0.32Si-0.004S-0.015P- 0.012Cr-0.002Mo-0.007Ni-0.02Cu- 0.028 Al -0.037Nb -0.008Ti- 0.001V, bal. Fe (wt. %). was determined using a Glow Discharge Optical Emission Spectrometer (GDOES), model Horiba GD. The steel plate, with dimensions, 300 x 30 x 10 mm, had three holes of 1 mm diameter and 5 mm depth drilled from the underside of the 10 mm thick substrate to place three thermocouples [26,27]. The holes divided the melted track into four sections each of 75 mm, Figure 2. Section1 was discarded due to the initial instability of the TIG torch, while section 3 (150mm from start of TIG processing) was used in the present investigation.

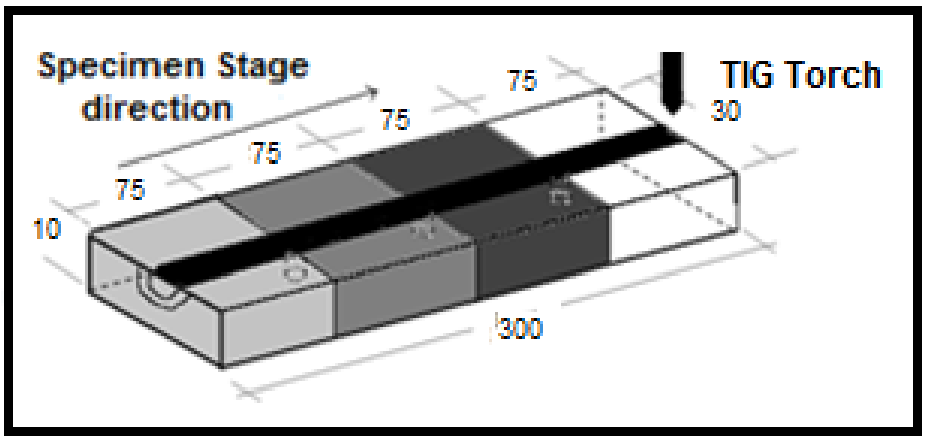

2 Schematic drawing showing in black the four sections of melt track, and the melting direction.

Figure 2 near here

The BM steel surface was ground on emery paper and degreased in acetone prior to the application of the preplaced powder. Both silicon (Si) powder 99.5% purity, with a nominal size of 45μm and silicon carbide (SiC) powder of 99.0% purity and nominal size of ~5 μm, were separately formed into a paste with a binder before application. Specimen 1 was coated with 1.0 mg mm^{-2} of SiC paste then dried at 80°C. For Specimen 2, Si paste was placed on the BM, dried at 80°C, and cooled to room temperature, after which 1.0 mg mm^{-2} of SiC paste was preplaced on the silicon coated steel specimen [13]. Specimen 3 consisted of a preplaced Si paste on the BM to create a Si coated steel, subsequently dried in a furnace at 80°C. The pastes were then incorporated into the BM steel by TIG processing.

A Miller Dynastry 300DX TIG equipment was used to generate an arc with a 2.4 mm diameter thoriated tungsten electrode. The electrode was direct current negative and the tip was ~1mm above the specimen surface, to guarantee a constant energy input (E) along the single melt track, using argon as a shielding gas at a constant flow rate of 10 $Lmin^{-1}$. Identical torch and computer controlled stage conditions of 80A current (I), 11 volts (V), and the speed 1.0 mms^{-1} (s), were used for the three specimens processed as shown in Figure 2. The energy input (E) was calculated using Equation 1

$$\boldsymbol{E = \eta \frac{V*I}{s}} \quad (1)$$

to be 420 J mm^{-1}, where η is the efficiency of energy absorption was taken as 48% for a TIG process [46].

Once the melting process was completed, the specimens were allowed to cool to room temperature prior to microhardness determination and microstructural analysis. Each specimen from just beyond the location of the second hole of section 3, shown in black in Figure 2, was prepared for metallographic analysis using the conditions described in the ASTM E3-01 standard.

Microhardness measurements were conducted following the procedures detailed in BS 1043-2 1993 and BS6507-1 1998, using a Mitutoyo MVK G1 microhardness tester with 200gf load and a 15s time delay. Readings were taken on the specimen cross-section, of the melt zone (MZ), the heat affected zone (HAZ) and the BM, starting at 0.1 mm from the MZ surface and taking measurements in a vertical distance at 0.2 mm apart, towards the centre of the BM. Specimens were prepared for metallographic analysis following ASTM E3-01 standards. The crystallographic characterization of phases developed in the re-solidified surface was obtained by X-ray diffraction, using a Bruker D8 Advance with Da Vinci equipment with a Cu (λ = 1.5406 Å) source x-ray tube, set to 40kV and 40mA,with a step size of 0.5s and the increment 0.02º. The 2-theta range measured was 20° -100º. XRD data from all these sources was characterized using the International Centre for Diffraction Data (ICDD) PDF-2 database incorporated in the XRD equipment, allowing indexing of the peaks. XRD spectra were recorded from the BM surface of the MA steel and from MZ surfaces of Specimens 1,2 and 3. In addition, a specimen of compressed ~5µm SiC particulates was studied for comparison.

An Olympus GX51 optical microscope and a Hitachi Su-6600 scanning electron microscope (SEM) with an Oxford Instruments INCA system with 80 mm XMAX SDD detector and a wavelength detector were used to record and chemically analyse the microstructure of the metallographic specimens. The XRD mapping was undertaken with a Dual-Beam SEM/FIB system, FEI Helios Nanolab 600i.

Results

Microhardness

The microhardness of the three specimens is shown in Figure 3. Specimen1 (SiC) in which previous work (26,27) showed that the SiC particulates dissolved, is seen to retain a hardness of ~700Hv to a depth of 1.25 mm, while Specimen 2 with the two preplaced layers has a maximum hardness of ~870Hv, decreasing to 720Hv at 0.2mm and 618Hv at 0.6mm, before dropping to 185Hv in the HAZ. The hardness for Specimen 3 with only the Si paste, recorded a maximum of 710Hv retained to 0.7mm, which also decreased to ~617Hv at 0.8mm. The highest hardness was found in the top 0.2mm of Specimen 2, which was ~18% greater than the maximum in Specimen1, where hardness values similar to Specimen 3 were recorded. The data shows microhardness differences between depths of 0.1mm and 0.2mm in Specimen 2, which could be associated with the avoidance in dissolution of SiC particulates close to the MZ surface.

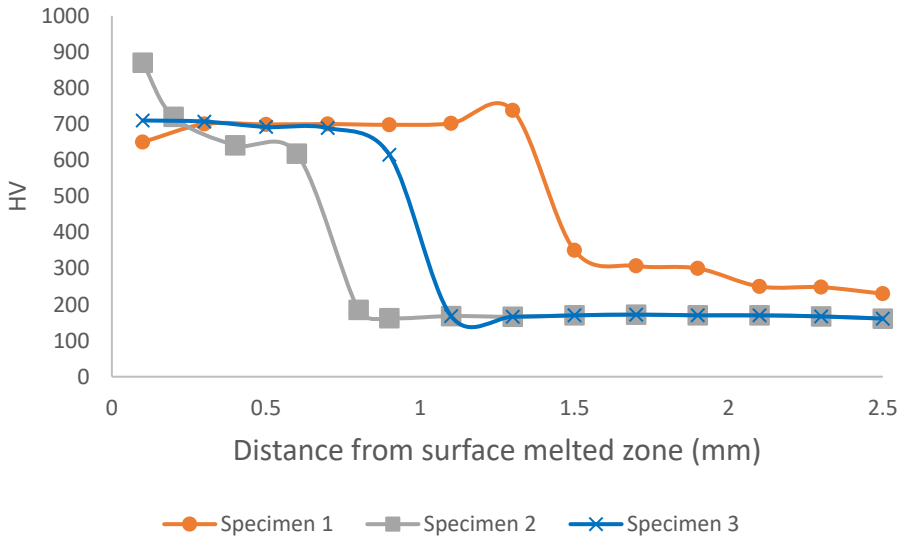

3 Microhardness of Specimens 1,2 and 3 as a function of distance from the melt zone surface.

X Ray Diffraction

Figure 4 allows a comparison of the XRD spectra from Specimens 1,2 and 3, with spectra from the BM, which shows only peaks corresponding to ferrite and cementite, and from the ~5μm size SiC powder. Figure 4 provides no strong evidence for the peaks corresponding to the SiC(p) peaks from Specimens 1 and 2. In this research, there is a distinct prospect of developing iron silicon phases and iron carbon silicon phases. However, there are peaks at 2θ of 22°, 33° and 41° in Specimen 2[G] which are not labelled. There is a possibility that several of these peaks may correspond to cementite, as the 2θ values in Specimen 2 at 33° and 41° appear to be displaced θ (020) and θ ((200) in the BM spectrum, and also for peaks at 61° and 84° being displaced θ (222) and θ (115).

For Specimen 3 in Figure 4 no matching was found with $Fe_3C(\theta)$ or ferrite (α). However, there is a reasonable matching with several of the peaks to gupetite, fcc (Fe_3Si). Of eight recorded peaks, only three have significant I/I_o ratios: F_{222} -100%, F_{400} -12%, and F_{422} - 19%. The other five peaks have I/I_o ratios ≤ 6%. This indicates that some of the labelled peaks in Figure 4 are complexes. Also, strong peaks at 2θ values of 62°and 74°, have not been associated with any of the phases considered here or in other work [10,30,47-50]. These peaks are present also in the spectrum recorded for Specimen 2. The PDF files used for the identification of these phases are given in Table1. In addition, around another 1000 files were checked including Si, ε-FeSi, Fe_2Si, Fe_3Si, Fe_5Si_3, FeSiC, Fe_8Si_2C, FeSiO,Fe_2SiO_4, SiO_2, austenite, NbC, VC, TiC, and iron oxides.

Table 1 PDF files chosen for the identification of the above phases

Phase		Powder Diffraction File Number
Austenite	(δ)	00-023-0298
Graphite	(G)	00-023-0064
Martensite	(α′)	01-044-1290

Fe_3Si	DO3 (F)	00-072-4250
FeSi	B2 (B)	
SiO_2	(S)	00-046-1242
Fe_3C	(θ)	00-003-0411
Ferrite	(α)	00-006-0696

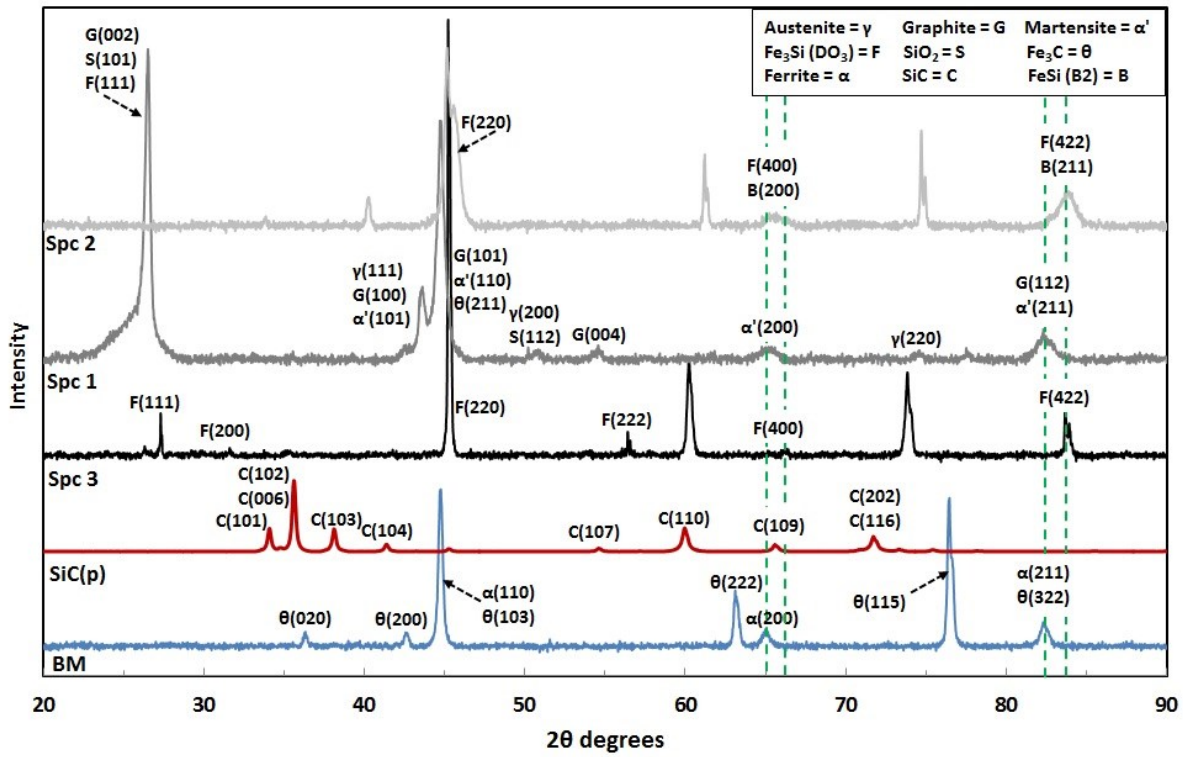

4 XRD spectra of Specimens,1,2 and 3, SiC powder and the BM MA steel.

Table 1 and Figure 4 near here

Microstructure

The same base metal (BM) was used for each of the TIG processed samples. Figure 5 is an SEM micrograph of the banded microstructure of BM, while Table 2 gives the EDX chemical composition of the area outlined.

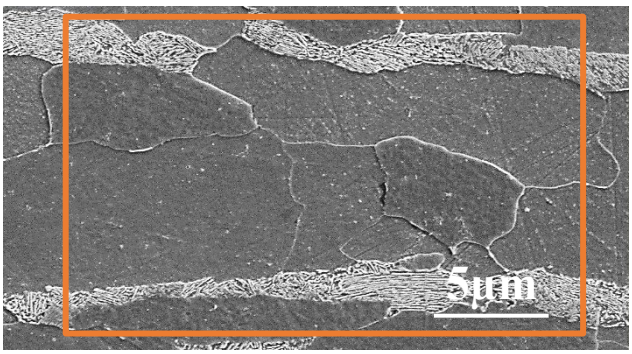

5 Microstructure of banded ferrite/pearlite in as- rolled microalloyed steel.

Table 2 Chemical composition (wt.%) obtained by EDX of the BM area outlined in Figure 5.

Spectrum	C	Si	Cr	Mn	Fe	Cu	Mo
1	4.78	0.52	0.00	1.10	93.60	0.00	0.00

The composition of the MA steel base metal (BM) determined by GDES was 0.14C-1.26Mn-0.32Si-0.004S-0.015P- 0.012Cr-0.002Mo-0.007Ni-0.02Cu- 0.028 Al - 0.037Nb -0.008Ti- 0.001V,bal.Fe (wt. %). Compared to the composition in Table 2, it is seen that the C content is overestimated by a factor of >30x, due mainly to contamination associated with the SEM, the specimen mounting compound and possibly etching methods. It is considered that an indication of the true carbon levels (as wt.%) in specimens where SiC dissolution has resulted in higher carbon levels being recorded, can be approximated by subtracting 4.64 (4.78-0.14) from the EDX carbon figures.

The data for Si also show an increase of ~1.6 times, while Mn in Table 2 is a little lower than that obtained by GDES.

Microstructure of Specimen 1

6 Optical micrograph of a transverse section of MZ in Specimen1 showing no cracking and no gross porosity.

Figure 6 is a transverse section of Specimen1 after etching in Nital, showing a variation in microstructures with depth, but no signs of cracking or porosity, which was confirmed by SEM. A higher magnification micrograph in Figure 7, shows a blocky needle phase which appears to be nucleating mainly from a grain boundary phase. EDX analysis is recorded in Table 3 from the positions indicated by arrows.

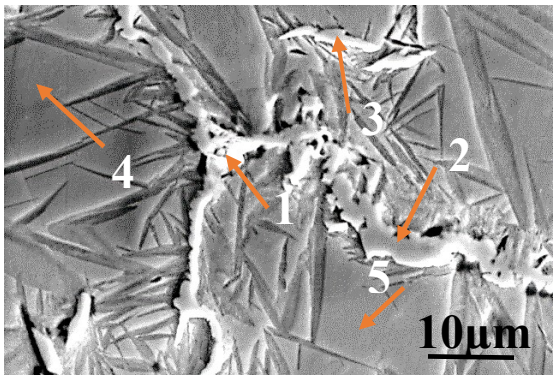

7 SEM micrograph from Specimen1showing a blocky needle phase contained within grains surrounded by a boundary phase. The arrows identify the positions from which EDX data given in Table 3 were taken.

Figure 7 is an SEM micrograph from Specimen1shows a blocky needle phase contained within grains surrounded by a boundary phase. The arrows identify the positions from which EDX data given in Table 3 were taken.

Spectrum 1 in the Table 3, indicates that the small particle is possibly associated with NbC; the BM analysis does include 0.037wt.%Nb. Also O and Mn are greater than in the other four spectra, which have Si levels < 3.00 wt.%. The C and Si levels in the boundary phase, spectra 2 and 3, are higher than in the needle matrix, spectra 4 and 5.

Table 3 Specimen 1 EDX compositional data for positions arrowed in Figure 7.

Spectrum	C	O	Si	P	Mn	Fe	Nb
1	13.27	4.16	1.39		3.19	76.51	1.47
2	8.06	1.91	2.87	0.57	1.87	84.72	
3	7.50	1.39	2.89		1.12	87.10	
4	5.79	1.35	2.57		1.06	89.23	
5	5.64	1.34	2.66		1.04	89.32	

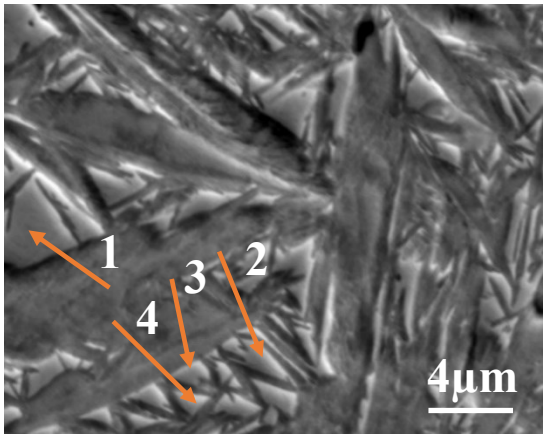

8 SEM micrograph of Specimen1with composition in Table 4 from regions indicated by arrows.

Figure 8 is an SEM micrograph from another area of Specimen1 showing just blocky needles, with composition given in Table 4 indicated by the four arrows.

Table 4. Specimen 1 EDX compositional data for positions arrowed in Figure 8.

Spectrum	C	O	Si	Mn	Fe
1	5.55	1.21	2.15	1.19	89.91
2	8.20	3.67	2.18	1.15	84.81
3	7.92	3.42	1.86	1.15	85.66
4	6.76	2.52	1.91	1.11	87.69

In Table 4, the Mn levels are very consistent, whereas the O varies by a ~3x between spectra 1, and those of 2 and 3. Again C varied significantly over very small distances, while Si was ~2wt.%. Figures 9 and 10 show microstructures observed in some parts of Specimen 1, the former being characteristic of a martensitic burst transformation, while that recorded in Figure 10 shows a eutectic, which could correspond to the Fe_3C peaks in Figure 4.

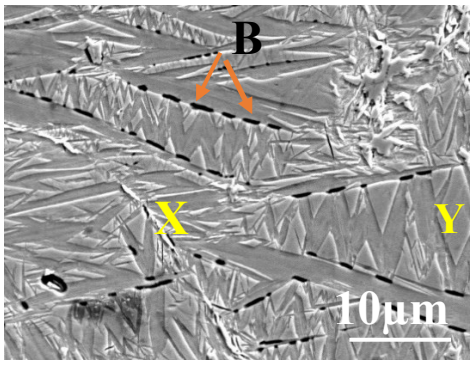

9 SEM micrograph of Specimen 1 showing blocky, often triangular shaped needles nucleating within larger needles such as X-Y, with sharp pointed ends, the boundaries of which are outlined by an interspersed black phase, B.

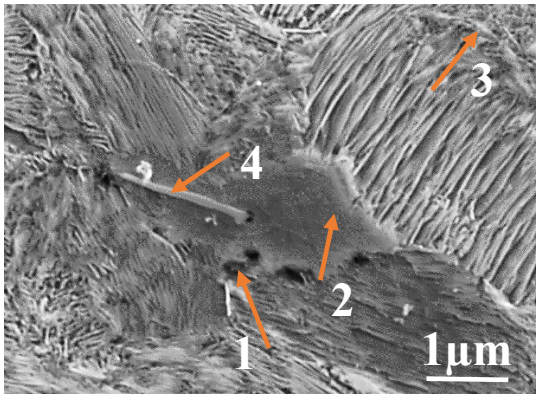

10 SEM micrograph of Specimen 1showing the positions in the eutectic area from which the compositional data of the four spectra shown in Table 5 were taken.

Table 5. Specimen 1 EDX compositional data for positions arrowed in Figure 10.

Spectrum	C	Si	P	Mn	Fe	Nb
1	6.20	1.08	0.39	2.12	86.79	3.41
2	5.98	1.42		2.52	90.08	
3	7.67	0.86		1.27	90.20	
4	5.99	1.30		2.13	90.58	

In Table 5, spectrum 1 was associated with the dark rounded shape (300 nm) indicated in Figure 10, and is another example of a NbC complex precipitate noted in Table 3,but here with some P and a lower Si level. Spectra 2 and 4 show similar compositions, whereas Spectrum 3 has the highest C and lowest Si and Mn levels. Oxygen was not recorded in any of the spectra.

Microstructure of Specimen 2

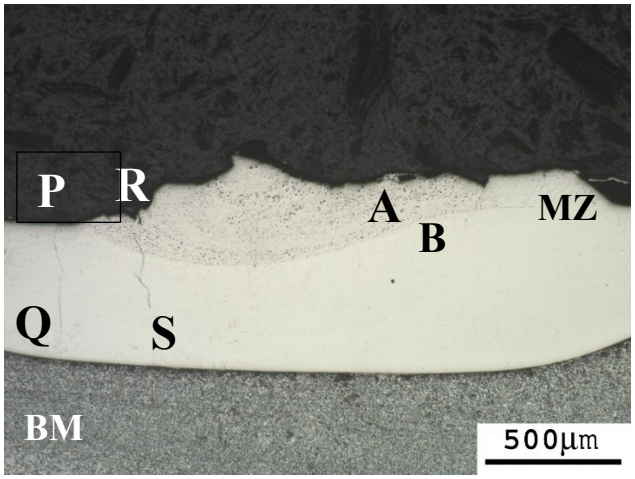

11 Optical macrograph of a transverse section of the MZ of Specimen 2.

Figure 11 is an optical macrograph of a transverse section of the MZ of Specimen 2, showing that it consists of two layers, A, a darker layer with an uneven surface, and B, a lighter coloured thicker layer. Thin cracks, PQ and RS, are apparent, spreading from the surface through layer A and part-way through layer B.

The higher magnification images of Specimen 2 in Figure 12, consist of four optical micrographs showing the two layers. The upper layer A, contains angular SiC particulates

and other phases, while in the lower layer B, no angular particulates, but other fine phases, are observed. In Figure 12(a), a thin surface region, T, containing a fine dispersion, is present above layer A. The matrix of layer A has darker segments, D, which in some areas appear to have formed on a boundaries interspersed in the lighter phase, containing small particles, such as those at S. The angular particulates are more in evidence closer to the top of Figure12(b). Details of layer B are shown in Figure12(c), where precipitates smaller than the angular particulates in layer A, outline grains. Figure 12(d) clearly shows the difference in size of the major precipitates in layers A and B.

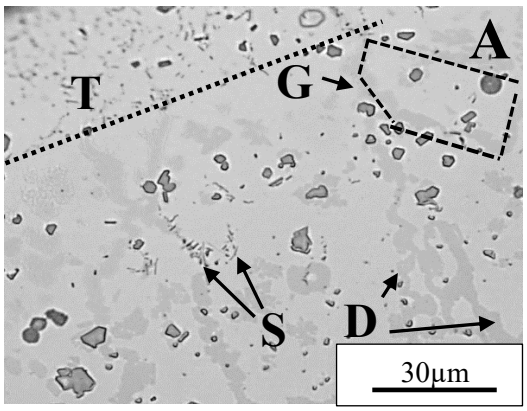

(a)

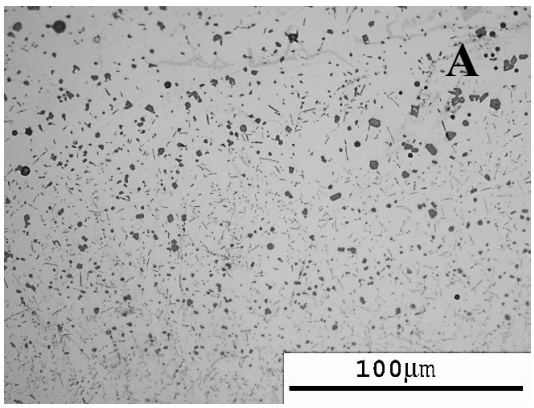

(b)

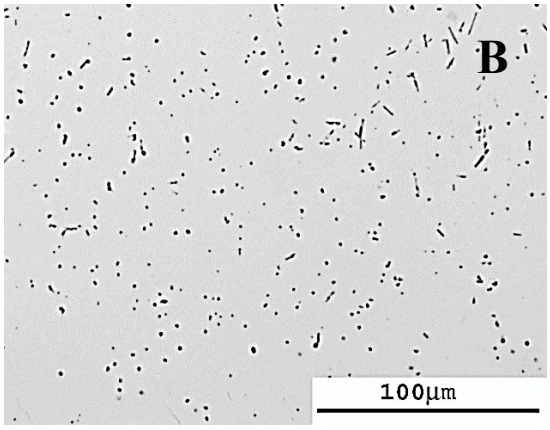

(c)

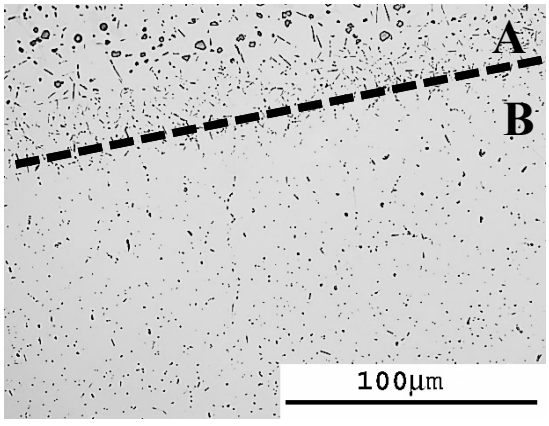

(d)

12 (a) Optical micrograph of layer A showing several phases in addition to SiC particulates. T is at the surface, with a fine precipitate dispersion, G outlines a darker coloured phase, also indicated by D, while S indicates a fine group of particles. (b) Optical micrograph of layer A showing several phases in addition to SiC angular particulates. (c) Optical micrograph of layer B showing particles outlining boundaries. (d) Optical micrograph showing the melt zone separated into two layers, the upper layer A containing SiC particulates, the lower layer B, with an absence of SiC particulates.

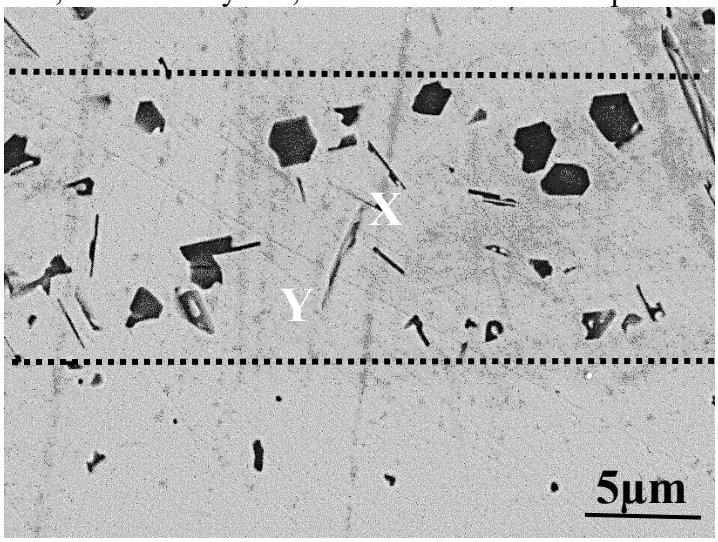

(a)

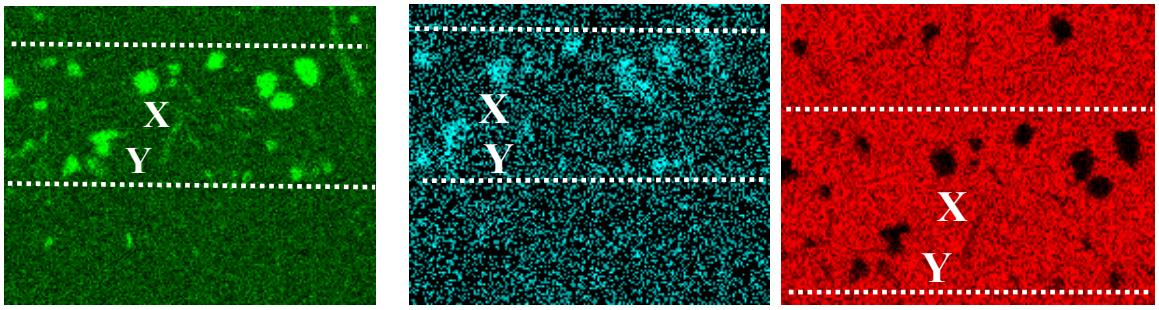

(b) Si_K (c) C_K (d) Fe_K

13 Secondary electron image of Specimen 2, (a) transverse section of melt zone (b) bright Si_K image of particulates (c) less bright image of C_K of particulates, (d) Fe_K showing dark image of particulates and red matrix of iron.

X-ray mapping was undertaken on the angular particulates observed in Figure 12a, b and d and thin needle precipitates in Figure 12c, to confirm if they were essentially SiC. Figures

13(b),13(c) and 13 (d), of particles present between the dashed lines in Figure 13a, show clearly the bright images of Si_k and C_k in the particulates and with lower intensities in the needles, such as XY. This change in intensity with morphology corresponds to EDX data from the two SiC morphologies present in Figure 14, where much higher Si_k, (~60wt.%) and C_k (~34 wt.%) present with lower Fe_k (~5 wt.%) data is recorded in Table 6 for the angular particulates arrowed 1 and 3, compared with the needles, arrowed 4 and 5 , < 25 wt.%,Si,12 wt.%, C with Fe >60 wt.%.The spherical particle arrowed 2,with 87wt.%C is considered to be graphite.

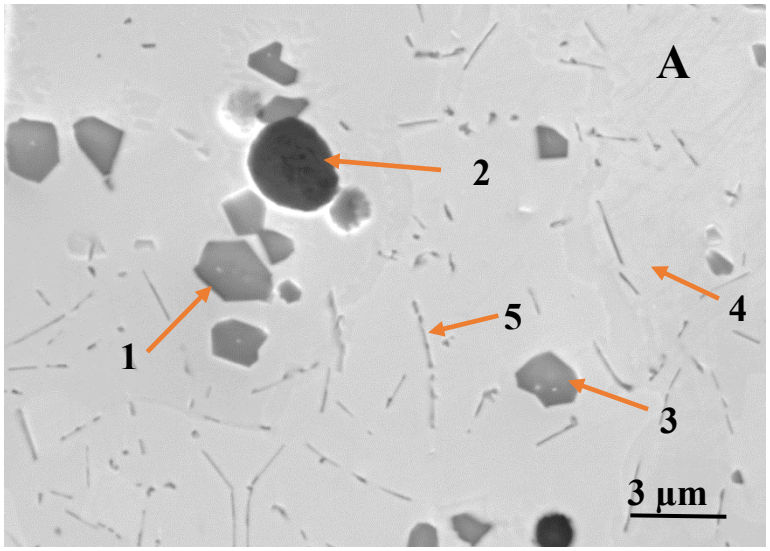

14 SEM micrograph of Specimen 2 showing an area close to the top of the MZ layer A.

Table 6. Specimen 2 EDX compositional data for positions arrowed in Figure 14.

Spectrum	C	O	Si	Mn	Fe	Si/C
1	33.57		61.23		5.21	2.19
2	87.03	2.80		1.41	8.76	
3	35.44		59.52		5.04	1.93
4	4.82		20.31	0.92	73.95	
5	11.76		24.93	0.62	62.70	

This is also the case for the needles, arrowed 2 and 3 in Figure 15a associated with an area of MZ in layer B. The corresponding EDX data recorded in Table 7 from the contaminated

rectangular area in Specimen 2, shows C levels three and two times respectively, greater than the ~4.0wt% derived from the arrowed 4 black rectangle within this area of the matrix. The Si levels in Table 7 are ~28 wt.% for the small particulates arrowed 1to 4 in Table 8, compared with ~17wt.%. for the needles in Figure15a.

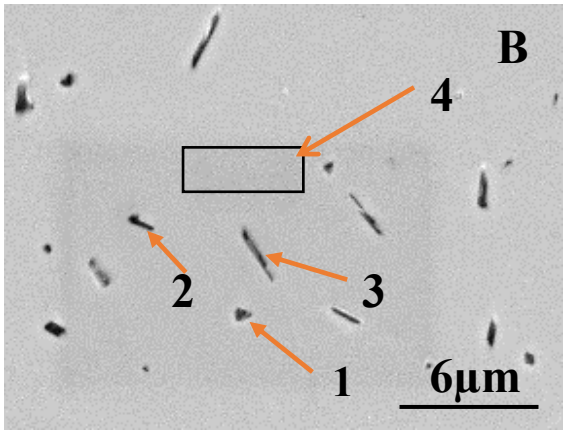

(a)

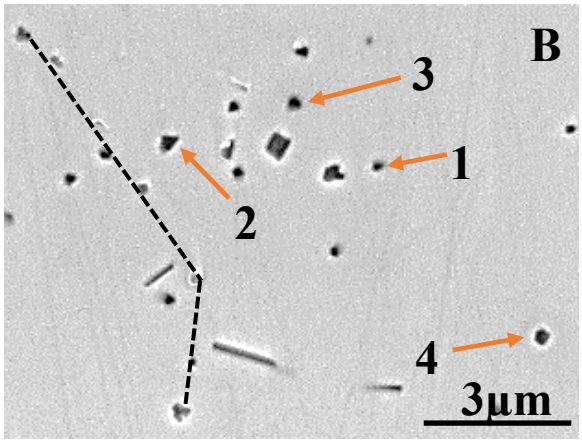

(b)

15

SEM micrographs of two areas in layer B of Specimen 2.
The arrows identify positions for EDX analysis given in Tables 7 and 8.

Table 7. Specimen 2 EDX compositional data for positions arrowed in Figure 15a.

Spectrum	C	Al	Si	Mn	Fe	Si/C
1	15.03	0.56	24.78	0.71	58.92	2.39

2	12.66	0.29	28.75	0.74	57.56	3.59
3	8.58		28.36	0.62	62.44	7.23
4	4.03		17.42	0.75	77.80	-

Figure 15 shows several Si rich precipitates, some outlining GB (dashed lines). Some ~100nm SiC cubes have been identified in the lower parts of the MZ, corresponding to layer B.

Table 8. Specimen 2 EDX compositional data for positions arrowed in Figure 15b.

Spectrum	C	Al	Si	Mn	Fe	Si/C
1	21.87		37.88		40.24	2.20
2	15.50	0.56	27.04	0.92	55.97	2.49
3	12.32	0.36	30.82	1.10	55.40	4.01
4	15.74	1.11	26.75	0.67	55.73	2.41

The Si/C ratio given in Table 8 was calculated by subtracting 4.64wt.% from the C data to account for contamination. The Si/C stoichiometric ratio is 2.33.

In Table 8, data confirms that the small angular morphologies arrowed as 1,2 and 4, in Figure 15b are essentially SiC particulates. Taking the Si wt.% given in Table 8 with the Si/C stoichiometric ratio of 2.33, the estimates of the carbon compositions for particle [1] of 17% [2]10.8%, [3] 7.7% and [4] of 11%C , are reasonable agreement with the respective carbon %. The MZ matrix composition given for spectrum 4 in Figure 15a has a C level similar to the MZ shown in Table 2, but with significantly higher Si and Fe levels. This trend also applies to data recorded from Specimen 1, presented in Tables 3, 4 and 5. It is noticeable that neither the angular particles, ~2-3μm in size, or the spherical graphite particles, seen in Figure 14, were observed in layer B.

Microstructure of Specimen 3

The macrostructure of Specimen 3 in Figure 16 appears almost featureless. A major crack is observed along UV and other minor cracks are present close to X and Y, indicating the brittle nature of this microstructure.

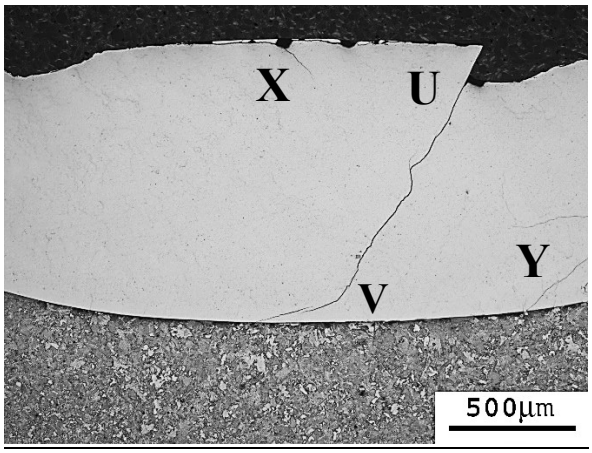

16 OM of Specimen 3 showing a crack UV from the surface through the MZ stopping at the HAZ.

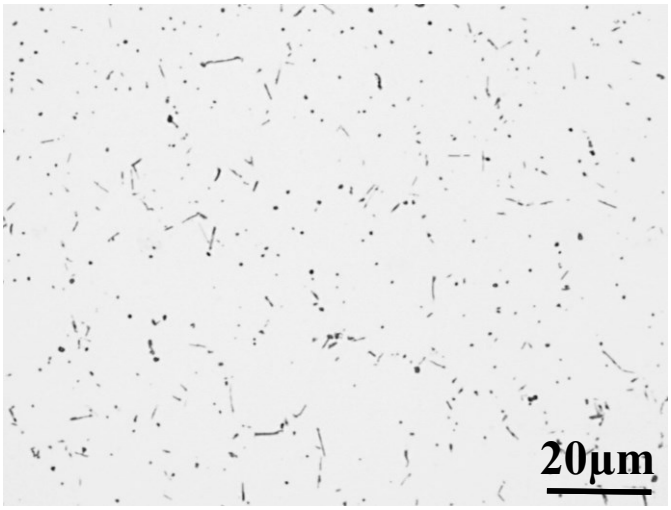

17 OM of Specimen 3 showing particles outlining grain boundaries.

Figure 17, is a higher magnification micrograph of an area below X and U in Figure 16,which shows that many precipitates outline boundaries of grains 5-20µm in size.EDX analysis of the precipitates was undertaken of regions shown in Figures 18 and 19, with the

corresponding data presented in Tables 9 and 10.The contrast in Figure 18 was arranged to highlight the grains,but produced the particles present on and within the grains in lower contrast.

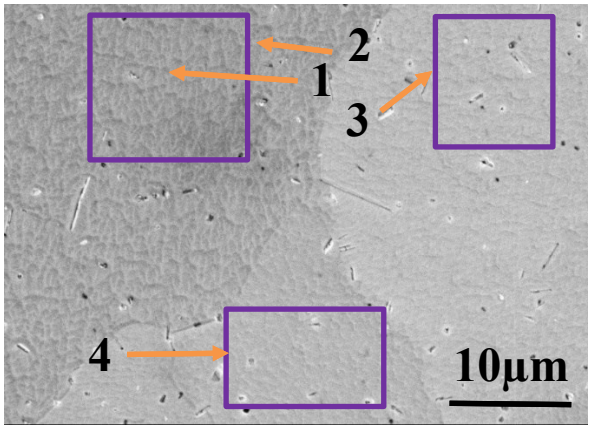

18 SEM micrograph of Specimen 3, showing position 1 and areas 2,3 and 4 from which EDX spectra where recorded to provide the compositional data given in Table 9.

The EDX data in Table 9 from areas 1,3 and 4 in Figure 18 is remarkably consistant and in agreement with the point analysis 2.

Table 9. Specimen 3 EDX compositional data for positions arrowed in Figure 18.

Spectrum	C	Si	Mn	Fe
1	4.80	17.06	0.83	77.31
2	4.49	17.54		77.97
3	4.53	17.84		77.63
4	4.38	17.46	0.79	77.36

A comparison of the carbon levels in Table 9 recorded for Specimen 3 shows that they are similar to those given for Specimen 1 in Table 2, while silicon data is similar to that collated in Tables 7 and 8 from Specimen 2.

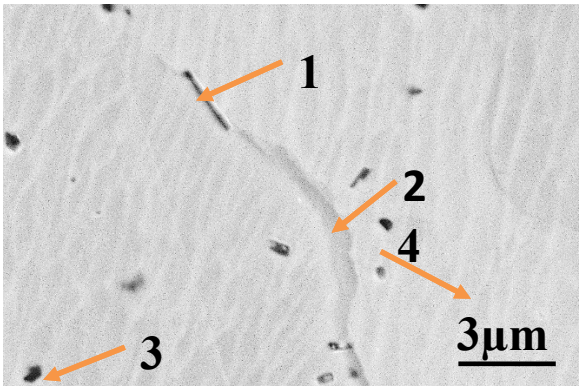

19 SEM micrograph of Specimen 3, with arrows showing a boundary and particles from which EDX spectra were recorded in Table 10.

In contrast to the areas analysed in Figure 18, two particles, arrowed 1,3 in Figure 19 were analysed and compared in Table 10, with the darker shade of boundary 2, and the matrix, arrowed 4. Particle 1 has a needle shape and contains the highest C and Si levels recorded. The matrix, 4, is closest in C and Si to the data in Table 9.

Table 10**.** Specimen 3 EDX compositional data for positions arrowed in Figure 19.

Spectrum	C	Si	Mn	Fe
1	13.76	23.43		62.81
2	4.75	21.11	0.77	73.38
3	5.93	20.96		73.10
4	4.99	18.97		76.04

The result of over 30 EDX analyses carried out on Specimen 3 shows a clear compositional divide into (a) the particles which contained ~14 C, 28-32Si, 0.65-0.97Mn, with some having ~0.40Al and (b) the matrix which contained 4.5-5.1C,14-23Si, ~0.60Mn (all in wt.%). This is similar to the EDX data of layer B Specimen 2.

Discussion

The application of TIG as an economic process for surface engineering is now well established [51]. A wide range of energy inputs (E) from 210Jmm^{-1} to 3479 Jmm^{-1} have been investigated [23-27]. The energy input must be sufficient to melt the base metal, thus allowing the ceramic particulate to be incorporated into the MZ, but normally insufficient energy to completely melt the ceramic. Also, porosity and cracking, which have been reported in some work, must be avoided [22, 33].

Following the laser or TIG processing of MA steels incorporating SiC particulates, increases in the hardness of the solidified MZ were noted[10,23, 24, 26, 27]. In the present work, single rows of indents were produced from the surface to the bottom of the solidified MZ [26]. It should be noted that many publications do not document the detailed methodology adopted to gather hardness data. Research similar to the present work includes that of Majumdar et al. [10], who recorded increases from a BM hardness of 190VPH to a MZ of ~600VPH [10], Buytoz [23] from 220 to 1135Hv,Patel et al[24] from 190 to 1253Hv, Muñoz de Escalona et al.[26,27], 200 to 800Hv, and Sharma et al.[52] 205 to 625Hv,the data depending on the energy input and particulate concentration. In addition, Majumdar [53] investigated the possibility of using laser surface alloying with silicon additions, raised the hardness of the BM of 150HV to 575HV.

Most of the increases in hardness were attributed to the formation of silicon phases. Tang et al. [30], who studied the solid state reaction zone between silicon carbide and iron in the temperature range from 800-1100°C (1073 to 1373K), recalled that there exist several iron silicides in the Fe-Si binary system, such as Fe_3Si, Fe_5Si_3, and ε-FeSi, all shown in Figure 1, which have been identified mainly through XRD spectra, Table 11. Several investigations base their identification on a single peak in the spectrum for which no hkl

indices are given and no attention paid to the intensity ratio, where other peaks with higher intensity ratios would be expected to be present for an analysis to be endorsed. In the present investigation, the initial procedure recommended by Rietveld [54] of ascertaining the 2θ position, which provided the corresponding hkl, and the peak height giving the intensity ratio, was followed. Table 1 collects together the phases 'identified' in a detailed search through the JCCD files: those providing the best match are recorded in Table 11. This also includes the space group, and to avoid the confusion noted by Jang and Choi [48], the three sets of symbols used in the literature to label some of the phases,

Table 11 near here

Table 11 Phases identified in the literature involving laser and TIG surface engineering of carbon steels incorporating SiC particulates.

Phase	Composition wt.% Si	Space group	Reference
Fe (Si) (γ)	0 to 10.9	$Fm\bar{3}m$	27,52
Fe (Si) (A2,α)	0 to 1.63	$Im\bar{3}m$	47
FeSi ($B2,\alpha_2$)	~5 to 12	$Pm\bar{3}m$	48, 54,62,63
Fe_3Si (DO_3,α_1)	~5 to 18	$Fm\bar{3}m$	23,30, 47,48,53,62,63
Fe_2Si	~ 20.1	$P\bar{3}m_1$	10,11, 37 ,47,53
Fe_5Si_3	23.2	$P6_3/mcm$	68
ε-FeSi	~34	$P2_13$	47,69
β-$FeSi_2$	53.4 to 58.2	P4/mmm	47
α-$FeSi_2$	50.2	Cmca	47
Si	100	$Fm\bar{3}m$	47
SiC			10,23,30
Fe_8Si_2C			49
$Fe_{0.78}Si_{0.09}C_{0.12}$			11
C (graphite)			28,30
Fe α'			27, 52

The solubility limit of SiC in molten Fe-Si-C alloys is well established [40-43]. Without appreciable quantities of silicon present in the liquid iron, silicon carbide dissolution will

clearly produce graphite saturation before silicon carbide saturation. The SiC, at a level of about 10 wt.%, made by Terry and Chinyamakobvu [28] was expected to dissolve totally in liquid iron. They showed that this occurred quickly and offered little expectation of retaining undissolved SiC, even by rapid processing in the liquid state.

From the literature, the melting points of interest in this work collated below are:

silicon 1414°C, iron 1535°C, silicon dioxide 1713°C, silicon carbide ~2700°C.

In the present study, following the TIG processing of the preplaced silicon and silicon carbide on the MA steel, a liquid rich in silicon will be produced around 1550°C, in which the silicon carbide particulates should then be incorporated, as occurred in Specimen1.

Figure 4 shows no peaks corresponding to SiC for either Specimen 1 or Specimen 2. However, the X-ray mapping of Specimen 2 in Figure 15, with the SEM/EDX investigation of the angular particles and needles seen in Figures 14 and 15, together with the corresponding data in Tables 6 to 8, clearly supports the view that SiC is present in layer A of Figures 12(a), (b) and (d). The absence of peaks corresponding to SiC in Figure 4, may be a function of the distribution, size and volume fraction of SiC precipitates sampled by the XRD experiments. Also in the present work SEM/EDX examinations were undertaken on specimen transverse sections while XRD spectra were collected from surfaces. While the hardness data recorded for Specimen1 has been attributed to the significant quantity of martensite [27], also detected by Sharma et al [52], this phase was not detected in the spectrum of Specimen 2 in Figure 4, or in any SEM studies, eg. Figures 12 to 15, The threefold increase in hardness in layer A of Specimen 2 over that of the BM, Figure 4, is attributed in part to the presence of angular particles observed in Figures12 a, b and d, Figure 13a and Figure 14, which show in Table 6, C and Si levels which strongly indicate that they are SiC particles. Also they are in a similar size range of 2-3μm to the initial SiC particulate addition. However, much smaller angular particles, 30-50nm in size, were observed in layer B, Figure 15b.These are associated

with much higher Fe contents, Table 7, than those in Figure 14, and may have precipitated during cooling from the TIG processing. Their formation requires some of the SiC particulates originally in layer A to have partially dissolved, and the Si and C atoms redistributed in layer B, possibly by Marangoni forces [54] which circulate material within the MZ. However, as a copious distribution of angular SiC particulates are still present in layer A, this suggests that the addition of Si does provide some protection for the SiC particulates, resulting in a limited dissolution. Kalogeropoulou et al. [55] have produced compelling evidence which shows that silicon additions produce a reduction in the contact angle between SiC and liquid iron, leading to an improvement of wetting, thereby reducing the reactivity between SiC and Fe. This effect was explained by the chemisorption of Si at the Fe/SiC interface.

While the Si addition in Specimen2 resulted in a reduction in SiC dissolution, giving a concomitant increase in hardness compared to that of the BM, it was not as effective overall as the SiC particulate addition alone in Specimen1. Here, the dissolution of SiC, with the corresponding increase in both Si and C atoms in the MZ, resulted in the formation of phases including martensite, graphite and a eutectic. These had a combined effect of producing a significant increase in hardness retained to a greater depth compared with that of the BM. In Specimen 2, the depth at which the highest hardness ~870Hv decreases to 720Hv at 0.2mm, coincides with the interface between areas A and B in Figure 12d.

It is well established that the presence of silicon in steel can destabilize cementite and promote the precipitation of graphite, and that dissolution of cementite will supply more carbon for the formation of graphite [56-59]. The presence of graphite has been recorded in Specimen 2, Figure 14, Table 6, and in Specimen3. It is suggested that the absence of cementite in the MZ of the three specimens considered here, Figure 4, reveals the source of the carbon for graphite growth.

Following TIG processing, both the cooling rate and the Si content in the MZ have a significant influence on the microstructure. The retardation of the precipitation of cementite by silicon can result in a carbide free bainite and retained austenite. The XRD spectra for Specimens 1,2 and 3, shown in Figure 4, have no peaks corresponding to ferrite, which would be present if the matrix was bainite, rather than the martensite detected in Specimen 1. Also there is little evidence in Figure 4 for the presence of cementite in Specimen1, although a eutectic, Figure 10, was observed in a few areas. But there are peaks at 2θ of 22°,33° and 41° of Specimen 1, which are not labelled. The possibility that several of these peaks may correspond to cementite was considered, as the 2θ values in Specimen1 at 33° and 41° could be displaced θ (020) and θ ((020) in the BM spectrum. The same can be said for Specimen1 peaks at 61° and 84° being displaced θ (222) and θ (115). However, the possibility of additions of Si influencing the peak positions of ferrite of Specimen1 in Figure 4, as discussed by Speich et al.[60] and by Huyan et al.[61], and of cementite, discussed by Okamoto and Kagawa [62], has been dismissed due to the lattice parameter changes being too small to affect the necessary changes in 2θ values. Several tests were undertaken with a control specimen to rule out the unidentified peaks being associated with the X-ray equipment or specimen preparation. Also, because the XRD spectra were gathered from the MZ surface, while the EDX spectra were collected from a transverse cross-section of the MZ, the phases present may not match exactly.

The macrograph Figure 6 of Specimen1shows no signs of cracks in the MZ, while cracking is present in the MZ's of Specimens 2 and 3, Figures 11 and 16. There are significant differences in the matrix Si content of the specimens. The maximum Si level given in Tables 3,4 and 5 for Specimen 1is 2.88 %. This compares with matrix levels of 20.3% for Specimen 2, spectrum 4 in Table 6 and 17.42% for spectrum 4 in Table 7, both having ~4wt% C. Similar levels were recorded for Specimen 3. The dotted line in Figure 1 shows that under

equilibrium conditions at levels of 17 to 20wt.% Si, several phase fields are passed through on cooling from the liquid to room temperature.

The observation of MZ cracks is considered to be associated with the significant increase in the Si % of the matrix recorded for both Specimens 2 and 3 compared to Specimen 1. It is well established that during the production of thin sheets for electromagnetic applications, at concentrations above 3.5 wt.%, the ductility of Fe–Si alloys is considerably reduced, making the material too brittle to normally be cold or hot-rolled without cracking [31]. This brittleness is attributed to the presence of an ordered phase. When the silicon content is higher than 3.5wt.%, two kinds of ordered structure, B2 (FeSi) (Pm3m), a=0.277nm, and DO3 (Fe_3Si) (Fm3m) a= ~0.564nm, are known to form in iron- based alloys, on the basis of the fundamental crystal lattice of bcc A2(Im3m) a = 0.2866nm [62-65]. Up to ~5.5wt.% Si, the B2 structure is formed from A2(disordered solid solution with bcc lattice) by unlike – atom pairing of the first neighbours.A further increase in silicon content leads to a phase transition towards ordered DO_3structure, through additional ordering between second nearest neighbouring atoms. In their work Starke et al [66] detected only the metal richest silicide, DO_3 Fe_3Si, which was considered to be due to the enthalpy being larger than that of SiC, making it thermodynamically favoured.

In Figure 4, the F peaks in the XRD spectrum of Specimen1 have been revised from the previous publication [27]; they are now labelled B2. With the inclusion of additional spectra in Figure 5, a 2θ shift of ~2° can be seen between the (200) peaks of Specimens 2 and 3 and those of Specimen1.This is repeated for the (400) and (422) peaks. With a lower Si content being recorded for Specimen1, the B2 FeSi phase is more likely to form, whereas the DO_3 phase is more likely to form at Si levels above 5.4wt%. In Figure 1, between 5.5 and 11.5wt.%Si, both phases can be observed[36] and have been explored by Matsumura et al.[67]. The broadening of the peaks is often associated with overlapping of two or more

peaks [68], and this was considered to be the case for B and F peaks [69], such as (400) and (422) of Specimen 3 in Figure 4.

Jung and Choi [48] and Ouyang et al. [70] noted the double diffraction which occurred by both B2 FeSi and DO_3 Fe_3Si phases, resulting in additional smaller peaks between the main peaks. These peaks become more prominent as the Si content of the Fe-Si-Cr alloys increased from 7 to 11 wt.% Si [48]. While small variations in the background spectra of the three specimens in Figure 4 is noted, they do not mirror these sharp peaks.

Most publications on Fe-Si steels containing $\geq$ 6.5wt.% Si,have been concerned with magnetic thin film development,where brittleness is less of a problem than in bulk iron silicides[71].One area which has considered ~9wt.% has been investigations involving the composition of the earth's core, in which B2 was reported as a prominant phase [72], and also after heat-treatment at 700°C, in a similar alloy [63]. This is in contrast to the present work, which found Fe_3Si DO_3 at higher Si levels,Tables 6-10.In identifying DO_3 in Figure 4, both spectra from both gupetite and suessite [73] were compared with the collected spectra; the former provided a slightly better agreement.

A probable explaination for the absence in cracking in Specimen1,where the FeSi phase has been identified as B2, follows from the work of Liang et al.[74].They found that by replacing the long-range order associated with the brittle DO_3 phase and developing the more ductile B2 FeSi phase, removed most cracking during cold rolling.

The XRD spectra in Figure 4 of Specimens 2 and 3 show peaks corresponding to the DO_3 phase, and unidentified peaks.The possibility of the latter being associated with higher Si phases,noted in the literature,Table11, was considered.

When Si content is >15wt.% ,both DO_3 Fe_3Si and ε -FeSi should form,and have been reported [10,11,37,47].However,some of these results are open to question, as the identification is

often lacking crucial aspects detailed by Rietveld [54]. XRD spectra have been recorded for Fe_2Si [37], Fe_5Si_3[75] and ε-FeSi [76]. ε-FeSi has only three 2θ peaks with intensity ratios ≥ 20%; at 45.3° (210) 100%, 50° (211) 40% and 80.6° (321) 20%. No peaks for Specimens 2 and 3 in Figure 4 are found corresponding to the last two 2θ values. The possible presence of the two high temperature phases Fe_2Si and Fe_5Si_3 was also considered, on the basis that a needle phase which fitted with the XRD peaks of martensite was found for Specimen1.This indicates that cooling rates ≥30°Cs^{-1}, were achieved following TIG processing. However, insufficient evidence for these phases is observed in Figure 4.

Therefore the main iron silicon phases, probably containing small levels of Fe, Mn and C, identified in Figure 4 are B2FeSi and DO3 Fe_3Si, which have a significant influence on the microhardness and brittle behaviour of the surfaces of the TIG process alloys studied in this research.

While the original concept applied in the present work of increasing the Si level in the TIG MZ of the MA steel surface, based on the research of Kawanishi et al. [43], did result in the retention of SiC particulates in layer A of Specimen 2, observed in Figures12 a, b and d, Figure 13a and Figure 14, this was accompanied by cracks. Cracks observed in the work of Liang et al.[74] were claimed to be due to a matrix of DO_3 Fe_3Si, which was also identified in XRD spectra in Figure 4.Reducing the Si level from 17wt.%, Table 7, to produce a MZ Si level of ~5.0 wt.%,accompanied by rapid cooling, may result in the development of a matrix of the less brittle B2FeSi phase, and eliminate major cracking,as found by Liang et al.[74]. This level should be sufficient to satisfy the wetting and coating of SiC particulates by Si, which was given as the reason for their retention by Kalogeropoulou et al. [56], resulting in a harder, crack-free MZ.

Conclusions

A comparison of particulate additions of SiC (Specimen1), Si+SiC (Specimen2) and Si (Specimen 3) on the microhardness and microstructure of the melt zone of a microalloyed steel of base metal hardness of 170- 200Hv, following surface engineering by tungsten inert gas torch processing to create a single molten track using an energy input of 420Jm^{-1}found that:

(1) Specimen 1, in which the SiC particulates had dissolved, increasing the carbon and silicon contents of the MZ liquid, solidified to give a layer of hardness of ~700Hv retained to a depth of 1.2mm. This was due to an inhomogeneous distribution of morphologies comprising a complex mixture blocky needle phase and a fine eutectic phase. The Si level determined by EDX was <3 wt.%. Peaks corresponding to martensite and B2FeSi were among those present in the XRD spectra. No cracking or porosity in the MZ were observed.

(2) Specimen2 resulted in two layers A and B. Layer A developed the highest hardness ~ 870Hv, which decreased to 720Hv at 0.2mm, coinciding with the layer boundary. Layer B retained a hardness of 618Hv to a depth of 0.6mm. SiC particulates of 2-3 μm size were observed in layer A, while smaller SiC precipitates of angular and needle shapes were present in layer B. These were identified by X ray mapping, but corresponding peaks were not present in the XRD spectrum, which did however contain peaks matching DO_3 Fe_3Si. The matrix Si level was ~17wt.%. Cracks from the surface through both layers were observed.

(3) Specimen 3 developed a MZ with a maximum hardness of 710Hv, decreasing to ~618Hv at 0.9mm, then dropping to the BM hardness of ~170Hv.XRD spectrum contained broad peaks which was interpreted as a complex of B2FeSi and DO_3Fe_3Si phases. The matrix Si level was ~17wt.%. Cracks were observed in the MZ.

(4) by optimizing the Si and SiC additions in Specimen 2, together with the TIG processing conditions, it may be possible to retain the SiC particulates, avoid the formation of the

brittle DO_3 Fe_3Si ordered phase, eliminate cracking and attain hardness values in the region of 1000Hv.

Acknowledgements

The authors would like to acknowledge that some of this work was carried out at the Advanced Materials Research Laboratory, housed within the University of Strathclyde. K. He and B. Wei acknowledge the financial support of the National Natural Science Foundation of China (No.51271202)

Disclosure statement

No potential conflict of interest was reported by the authors

References

[1] Taya M, Arsenault RJ. Metal matrix composities- themomechanical behaviour. Pergamon Press, Oxford,1989

[2] Gurcan AB, Baker TN. Wear behavior of AA6061 aluminum-alloy and its composites.Wear,1995;188:185-191.

[3] Ayers JD, Bolster RN. Abrasive wear with fine diamond particles of carbide-containing aluminum and titanium-alloy surfaces. Wear. 1984; 93:193-205.

[4] Selamat MS, Watson LM, Baker TN. XRD and XPS studies on surface MMC layer of SiC reinforced Ti-6Al-4V alloy. J. Mater. Pro. Technol.2003;142: 725-737.

[5] Mridha S, Baker T.N. Metal matrix composite layers formed by laser processing of commercial purity Ti-SiCp in nitrogen environment. Mater. Sci. Technol. 1996;12: 595-602.

[6] Mridha S, Baker TN. Metal matrix composite layer formation with 3 mu SiCp powder on IMI318 titanium alloy surfaces through laser treatment J. Mater. Pro. Technol.1997; 63: 432-437.

[7] Ion JC, Laser processing of engineering materials. Elsevier, Amsterdam,2005,261-326.

[8] Zhong M, Liu W. Laser surface cladding: the state of the art and challenges. Proc. Inst. Mech. Eng. Part C. J Mech Eng Sci. 2010; 224:1041-1062.

[9] Gemelli E, Gallerie A, Caillet M. Improvement of resistance of oxidation by laser alloying on a tool steel surface. Scripta Mater. 1998; 39: 1345-1352.

[10] Majumdar JD, Chandra BR, Nath AK, Manna I. Studies on compositionally graded silicon carbide dispersed composite surface on mild steel developed by laser surface cladding.J.Mater.Proc.Technol.2008;203:505–512.

[11] Thawari G, Sundararajan G, Joshi SV. Laser surface alloying of medium carbon steel with $SiC_{(p)}$.Thin Sol Films. 2003; 423:41-53.

[12] Khan TI, Fowles D. The surface modification of a Ti-6Al-4V alloy using a metal arc heat source, Surf.Eng.1997;13:257-259

[13] Mridha S, Ng BS. Addition of ceramic particles to TIG melted titanium surfaces,Surf.Eng.1999;13:210-215.

[14] Mridha S, Ong H S, Poh L S, Cheang P. Intermetallic coatings produced by TIG surface melting, J. Mater. Proc. Technol. 2002; 113:516-520.

[15] Amado J M, Tobar MJ, Alvarez JC, Lamas J, Ya´n˜ez A. Laser cladding of tungsten carbides (Spherotene1) hardfacing alloys for the mining and mineral industry. Applied Surface Science. 2009; 255: 5553–5556

[16] Kang A S, Cheem G S, Singh G. Wear behavior of hardfacings on rotary tiller blades. Procedia Eng. 2014; 97:1442 –1451.

[17] Bartkowski D, Bartkowska A. Wear resistance in the soil of Stellite-6/WC coatings produced using laser cladding method. Inter. J Refractory Metals Hard Mater,2017; 64: 20-26.

[18] Rostami J, Chang S H. A Closer Look at the Design of Cutterheads for Hard Rock Tunnel-Boring Machines. Engineering,2017; 3: 892–904.

[19] Urminský J, Zaujec R. Analysis of hardfacing and milling of forging die by CAx Technologies. Mater. Sci. Forum, 2018; 919:354-361.

[20] Wang XH, Song Sl, Zou ZD, Qu SY. Fabricating TiC particles reinforced Fe-based composite coatings produced by GTAW multi-layers melting process. Mater Sci Eng A. 2006;441:60-67.

[21] Mridha S, Baker T N. Overlapping tracks processed by TIG melting TiC preplaced powder on low alloy steel surfaces. Mater Sci Technol. 2015; 31: 337-343.

[22] Sahoo C K, Soni L, Masanta M. Evaluation of microstructure and mechanical properties of TiC/TiC-steel composite coating produced by gas tungsten arc (GTA) coating process.Surf.Coat.Technol.2016;307:17-27.

[23] Buytoz S. Microstructural properties of SiC based hardfacing on low alloy steel. Surf Coat Technol.2006; 200:3734– 3742.

[24] Patel P, Mridha S, Baker TN. Influence of shielding gases on preheat produced in surface coatings incorporating SiC particulates into microalloy steel using TIG technique. Mater Sci. Technol.2014; 30: 1506-1514.

[25] Reddy GS, Arul S, Sellamuthu R. Improving surface hardness of mild steel plates by addition of silicon carbide using gas tungsten arc as heat source. Appl Mech Mater. 2014;592-594: 879-882.

[26] Muñoz de Escalona P, Mridha S, Baker TN. Effect of silicon carbide particle size on the microstructure and properties of a coating layer on steel produced by TIG technique. Adv Mater Proc Technol. 2016**;** 2**:** 451-460.

[27] Muñoz-Escalona P, Sillars F, Morrocco T, Edgar R .Mridha S, Baker TN.Silicon carbide particles incorporated into microalloyed steel surface: microstructure and properties Mater. Sci. Technol. 2020; 36:17-32.

[28] Terry BS, Chinyamakobvu OS. Assessment of the reaction of SiC powders with iron – based alloys. J. Mater. Sci, 1993; 28: 6779-6784.

[29] Pelleg J. Reactions in the matrix and interface of Fe-SiC metal matrix composite system. Mater, Sci. Eng.,1999; A269: 225-241.

[30] Tang W M, Zheng ZX, Ding HF, Jin ZH. A study of the solid state reaction between silicon carbide and iron. Mater Chem Phys.2002;74: 258-264.

[31] www.dierk-raabe.com/electrical-steels-fe-3-si

[32] Tang W M, Zheng ZX, Ding HF, Jin ZH. Control of the interface reaction between silicon carbide and iron. Mater Chem Phys. 2003; 80:360-365.

[33] Čikara D, Rakin M, Todic´ A. Cast steel–SiC composites as wear resistant materials. FME Trans. 2009; 37: 151–155.
[34] Contin A, Vasconcelos G de, Barquete DM, Campos RA, Trava-Airoldi VJ, Corat EJ. Laser cladding of SiC for diamond deposition on steels substrates. Diam. Rel. Mater.2016;65:105-114.
[35] Zhang C, Pei S, Ji H, Cui Y, Li M. Fabrication of Ni60–SiC coating on carbon steel for improving friction, corrosion properties. Mater Sci Technol.2017; 33,446-4.
[36] Kubaschawski O. Iron-binary phase diagrams. Springer-Verlag. New York,1982.
[37] Forbes A W, Dulal RP, Bhattarai N, Pegg IL, Philip J. Experimental realization and magnetotransport properties of half-metallic Fe22Si.J Appl.Phys.2019;15:243902.
[38] Ohnuma I, Abe S, Shimenouchi S, Omori T, Kainuma R, Ishida K. Experimental and Thermodynamic Studies of the Fe-Si Binary System. ISIJ Int.2012; 52:540-548.
[39] Cui S, Jung I H. Critical reassessment of the Fe-Si system. Calphad.2017;56:108-125.
[40] Raghavan V, Ghosh G. The carbon-iron-silicon system J. Alloy Phase Diagrams, 1986; 2:77
[41] Lacaze J, Sundman B. An Assessment of the Fe-C-Si System. Metall. Trans A 1991;22A: 1991—2211.
[42] Miettinen J. Reassessed thermodynamic solution phase data for ternary Fe-Si-C system. Calphad.1998;22:231-356.
[43] Kawanishi S, Yoshikawa T, Tanaka T. Equilibrium phase relationship between SiC and a liquid phase in the Fe-Si-C system at 1523-1723K. Mater. Trans.2009; 50:806-813.
[44] Shin JP, Young EL. Assessment of Mn-Fe-Si-C Melt in Unified Interaction Parameter Formalism. Metall. Mater. Trans B.2016;47:216-227.
[45] Zheng WS, Lu XG, He YL, Li L. Thermodynamic modelling of Fe-C-Mn-Si alloys. J Iron Steel Res.Int.2017;21:190-197.
[46] Easterling KE. Introduction to Physical Metallurgy of Welding, 1992, Butterworth-Heinemann, London.
[47] Lomovsky O I, Golubkova G V,Yadroitsev I,Smurov I. Laser-induced reaction of Si powder with a steel substrate. Inorganic Mater.2012; 48:263-266.
[48] Jang P, Choi G. Effects of silicon content on the properties of gas-atomized Fe-Si-Cr powders. IEEE Trans Mags. 2017;53: 2002705.
[49] Pei YT, Ouyang JH, Lei TC, Zhou Y. Microstructure of lase-clad SiC-(Ni alloy) composite coating. Mater.Sci.Eng.1995; A194:219-224.
[50] Lin Y-C, Chen H-M, Chen Y-C. Analysis of the microstucture and wear performance of SiC clad layer on SKD61 die steel after gas tungsten arc welding. Mater.Des.2013;47:828-835.
[51] Azwan M, Maleque M A, Rahman M M. TIG torch surfacing of metallic materials - a critical review. Trans. Inst. Metal Finish.2019;97: 12-21.
[52] Sharma D, Ghosh PK, Anant R, Kumar S. Surface modification of microalloyed steel by silicon carbide reinforcement using tungsten inert gas arcing. Mater. Res. Exp. (2019); 6:036530
[53] Majumdar JD. Development of in-situ composite surface on mild steel by laser surface alloying with silicon and its remelting. Surf. Coat. Technol. 2010; 205:1820-1825.
[54] Rietveld HM. A profile refinement method for nuclear and magnetic structures. J. Appl. Cryst. 1969; 2: 65–71.
[55] Mills KC, Keene BJ, Brooks RF, Shirali A. Marangoni effects in welding. Proc. R. Soc. London A1998; 356A: 911–925.
[56] Kalogeropoulou S, Baud L, Eustathopoulost N. Relationship between wettability and reactivity in Fe/SiC system. Acta metall, mater. 1995; 43: 907-912.

[57] He K, Brown A, Brydson R, Edmonds DV. Analytical electron microscope study of the dissolution of the Fe_3C iron carbide phase (cementite) during a graphitisation anneal of carbon steel. J Mater Sci.2006;41: 5235–524.

[58] Kozeschnik E, Bhadeshia H. K. D. H. Influence of silicon on cementite precipitation in steels. Mater. Sci. Technol. 2008; 24: 343-347.

[59] Gao J X, Wei B Q, Li D D, He K. Nucleation and growth characteristics of graphite spheroids in bainite during graphitization annealing of a medium carbon steel. Mater. Charact.,2016;118:1–8.

[60] Speich GR, Schwoeble, Leslie WC. Elastic-constants of binary iron-base alloys. Met.Trans. 1972;3:2031-2037.

[61] Huyan F, Larker R, Rubin R, Hedström P. Effect of Solute Silicon on the Lattice Parameter of Ferrite in Ductile Irons. ISIJ Internal.2014;54:248-250.

[62] Swann P R, Granas L, Lehtinen B. The B2 and DO3 Ordering Reaction in Iron–Silicon Alloys in the Vicinity of the Curie Temperature, Met. Sci., 1975;9: 90–96.

[63] Ustinovshchikov Y I, Sapegina I V. Ordering of Fe–Si Phases. Inorg. Mater.2005; 45: 24–31.

[64] Cava R D. Botta WJ, Kiminami CS, Olzon-Diobysio M, Souza SD, Jorge Jr AM, Bolfarini C. Ordered phases and texture in spray-formed Fe–5wt%Si. J Alloy Cpds. 2011; 509S:S260-S264.

[65] Cai C, Li C, Cai B, Wang Q. An experimental investigation on B2 phase transfer and grain boundary character on mechanical properties of rapidly cooled Fe-6.5wt.%Si alloy. J.Mater.Res.2018;33:507-515.

[66] Starke U, Weiss W, Kutschera M, Bandorf R, Heinz K. High quality iron silicide films by simultaneous deposition of iron and silicon on Si (111). J Appl. Phys.2002; 91: 6154-6161.

[67] Matsumura S, Tanakab Y, Kogac Y, Okid K. Concurrent ordering and phase separation in the vicinity of the metastable critical point of order – disorder transition in Fe – Si alloys. Mater. Sci.Eng.2001; A312:284 – 292.

[68] Cullity B.D. Elements of X-ray diffraction. Addison-Wesley Publishing Company, USA,1978.

[69] Kasama A H , Machado R ,Yavari AR , Vaughan G , Bolfarini C ,Kiminam CS, Botta Filho WJ. Order/Disorder Transformations in Spray Formed FeSiAl Alloys. J.Meta. Nano. Mater.2004; 20-21: 553-556.

[70] Ouyang G, Jensen J, Macziewski CR, Ma T, Meng F, Lin Q, Zhou L, Kramer M, Cui J.Characterization of ordering in Fe-6.5%Si alloy using X-ray, TEM and magnetic TGA methods.Mater.Char.2019;158:109973.

[71] Ouyang G, Chen X, Jiang Y, Macziewski C, Cui J. Review of Fe-6.5wt% Si high silicon steel-A promising soft magnetic material for sub-kHz application. J. Magn. Magn.Mater.2019;481:234-250.

[72] Fischer RA, Campbell AJ, Caracas R, Reaman DM, Dera P, Prakapenka VB. Equation of state and phase diagrams of Fe-16Si alloy as a candidate component of Earth's core. Earth Planet. Sci.Lett.2012; 357-358:268-276.

[73] Keil K, Berkley JL, Fuchs LH. Suessite, Fe3Si: a new mineral in the North Haig urelite. Am. Mineral.1982;67:126-131.

[74] Liang YF, Lin JP, Ye F, Li YJ, Wang YL, Chen GL. Microstructure and mechanical properties of rapidly quenched Fe–6.5wt.% Si alloy. J Alloys Compds.2010;504S: S476–S479.

[75] https://materialsproject.org/materials/mp-449/ fe5Si3

[76] Wang X, He Z, Xiong S, Wu X, Synthesis of crystalline pyramidal ε-FeSi and morphology- and size-dependent ferromagnetism. J. Phys. Chem. C. 2014; 118:2222-2228.

Figure Captions

1 The Fe-Si equilibrium phase diagram [36]

2 Schematic drawing showing in black the four sections of melt track, and the melting direction.

3 Microhardness of Specimens 1,2 and 3 as a function of distance from the melt zone surface

4 XRD spectra of Specimens,1,2 and 3, SiC powder and the BM MA steel.

5 Microstructure of banded ferrite/pearlite in as- rolled microalloyed steel.

6 Optical micrograph of a transverse section of MZ in Specimen1 showing no cracking and no gross porosity.

7 SEM micrograph from Specimen1showing a blocky needle phase contained within grains surrounded by a boundary phase. The arrows identify the positions from which EDX data given in Table 3 were taken.

8 SEM micrograph of Specimen1with composition in Table 4 from regions indicated by arrows.

9 SEM micrograph of Specimen 1showing blocky, often triangular shaped, needles nucleating within larger needles such as X-Y, with sharp pointed ends, the boundaries of which are outlined by an interspersed black phase.

10 SEM micrograph of Specimen 1showing the positions in the eutectic area from which the compositional data of the four spectra shown in Table 5 were taken.

11 Optical macrograph of a transverse section of the MZ of Specimen 2.

12(a) Optical micrograph of layer A showing several phases in addition to SiC particulates. T is at the surface, with a fine precipitate dispersion, G outlines a darker coloured phase, also indicated by D, while S indicates a fine group of particles. (b) Optical micrograph of layer A showing several phases in addition to SiC angular particulates. (c) Optical micrograph of layer B showing particles outlining boundaries. (d) Optical micrograph showing the melt zone separated into two layers, the upper layer A containing SiC particulates, the lower layer B, with an absence of SiC particulates.

13 Secondary electron image of Specimen 2, (a) transverse section of melt zone (b) bright Si_K image of particulates (c) less bright image of C_K of particulates, (d) Fe_K showing dark image of particulates and red matrix of iron.

14 SEM micrograph of Specimen 2 showing an area close to the top of the MZ layer A.

15 SEM micrographs of two areas in layer B of Specimen 2.
The arrows identify positions for EDX analysis given in Tables 7 and 8.

16 OM of Specimen 3 showing a crack UV from the surface through the MZ stopping at the HAZ.

17 OM of Specimen 3 showing particles outlining grain boundaries.
18 SEM micrograph of Specimen 3, showing position 1 and areas 2,3 and 4 from which EDX spectra where recorded to provide the compositional data given in Table 9.
19 SEM micrograph of Specimen 3, with arrows showing a boundary and particles from which EDX spectra were recorded in Table 10.